ELSEVIER

International Journal of Heat and Fluid Flow 19 (1998) 358–367

International Journal of HEAT AND FLUID FLOW

Mixed convection over a heated horizontal surface in a partial enclosure

V.V. Calmidi, R.L. Mahajan *

Department of Mechanical Engineering, University of Colorado, Campus Box 427, Boulder, CO 80309-0427, USA

Received 28 July 1997; accepted 6 January 1998

Abstract

This paper reports a numerical study of mixed convection on a heated horizontal surface within a partially open vertical enclosure in which the buoyancy driven and the forced flows oppose each other. Two values of the Grashof number, 10^4 and 10^5, are considered. Two kinds of analyses are performed: One in which the domain is considered to be symmetric by the imposition of appropriate symmetry conditions, and the other in which the full domain is simulated. For $Gr = 10^4$, both the symmetric and the full domains give rise to identical solutions and no multiple steady states are obtained. For $Gr = 10^5$, multiple steady state solutions arise with both the symmetric domain and the full domains. However, the hysteresis effect observed while using symmetric domain is not observed with the full domain. Further, the full domain analysis reveals interesting asymmetries that have been observed experimentally in a similar configuration in the past. The effect of the location of the exit boundary is also investigated. Results indicate that unless proper exit conditions are chosen, the quantitative results can vary considerably.

Keywords: Enclosure; Mixed convection; Multiple steady states

Notation

c_p	specific heat at constant pressure (J/kg K)
g	acceleration due to gravity (m/s^2)
Gr	Grashof number $= g\beta(t_w - t_\infty)L^3/\nu^2$
h	average heat transfer coefficient (W/m^2 K)
h_x	local heat transfer coefficient (W/m^2 K)
H	height of enclosure (m)
k	thermal conductivity (W/m K)
L	length of the horizontal surface (m)
Nu	average Nusselt number along horizontal surface
p	pressure (N/m^2)
P	non-dimensional pressure $= p/\rho u_c^2$
Pr	Prandtl number ν/α
q_x	local heat flux (W/m^2)
Re	Reynolds number $v_o L/\nu$
t	temperature (K)
T	non-dimensional temperature $= (t - t_\infty)/(t_w - t_\infty)$
u,v	velocity components in x,y directions (m/s)
U,V	non-dimensional velocity components $= u/u_c$, v/u_c
u_c	characteristic velocity due to buoyancy $= \sqrt{g\beta(t_w - t_\infty)L}$
x,y	space coordinates
X,Y	non-dimensional space coordinates
w^*	non-dimensional height of enclosure $= W/H$
W	height of outlet opening (m)
α	thermal diffusivity $= k/\rho c_p$ (m^2/s)
β	coefficient of thermal expansion $= -(1/\rho)(\partial\rho/\partial t)_p$
ν	kinematic viscosity (m^2/s)
ρ	density (kg/m^3)
τ	non-dimensional time

Subscript

o	inlet
∞	reference (ambient)
w	hot surface
x	local (along x-direction)

1. Introduction

Combined forced and natural convection occurs in many natural and technological processes. See Gebhart et al. (1988) for a general review. Mixed convection in enclosures and partial enclosures has gained importance in the recent past, especially in the thermal management of electronics (Petersen and Ortega, 1990; Rahman and Carey, 1990; Chen et al., 1991; Papanicolaou and Jaluria, 1994, and more recently Hsu et al., 1997). One configuration of interest is shown in Fig. 1. It is a close approximation of the flip-chip cooling configuration without the high performance heat sink. This configuration has been studied in detail by Angirasa and Mahajan (1995) with the direction of the flow reversed, i.e., mixed convection with aiding buoyancy and forced flows. However, the transport issues are expected to be significantly different and

* Corresponding author.

0142-727X/98/$19.00
PII: S0142-727X(98)00002-2

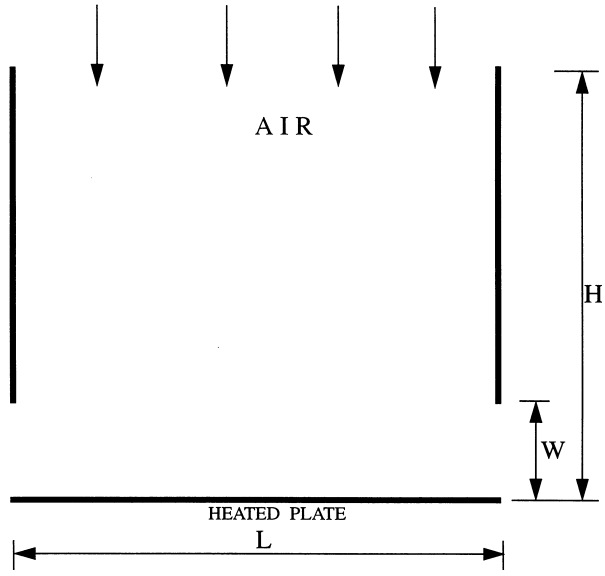

Fig. 1. Geometry of the configuration.

more complex for opposing buoyancy and forced flows, which is the focus of the present study.

Apart from electronic packages, the flow configuration is also encountered in a slightly modified manner in metal–organic chemical vapor deposition (MOCVD) reactors (Kelkar et al., 1996). Fluid flow and transport in MOCVD reactors have been investigated for typical operating conditions (see Kelkar et al., 1996; Patnaik et al., 1989; Fotiadis et al., 1987; Kelkar, 1996; Weber et al., 1990). In a number of these studies, multiple steady state solutions were observed for a certain range of operating parameters. For example, Kelkar (1996) studied the effect of aspect ratio, and wall boundary conditions on the multiple steady states. Weber et al. (1990) modeled flow in a vertical vapor-phase-epitaxy (VPE) reactor using a 2-D domain. They noted that stable asymmetric solutions exist for certain conditions. They present a bifurcation diagram which gives changes in flow types as a function of the heat flux. Mahajan (1996) noted that the study of such bifurcation phenomena is one of the areas of fundamental interest in mixed convection. Asymmetries in MOCVD reactors have been observed experimentally in the past (de Keijser et al., 1988; Roksnoer et al., 1989).

Calmidi and Mahajan (1995) observed hysteresis for the configuration shown in Fig. 1. Simulations were performed using a finite-difference code based on the ADI method. They noted that if a buoyancy induced cell already existed in the enclosure, it persisted for long before disappearing. On the other hand, an established forced flow was shown to inhibit the formation of the buoyancy induced cell. They also found that as the non-dimensional exit opening, w^* increased from $w^* = 0.2$ to $w^* = 0.4$, the hysteresis loop shifted. Upon further increase of w^* to 0.6, the hysteresis loop widened. In addition, unsteady behavior was observed. A buoyancy cell formed over the hot surface which was periodically flushed out by the incoming forced flow. However, these results were obtained by using a symmetric domain which is not capable of revealing asymmetric flows which might exist.

The objective of this paper is to present comprehensive numerical results for the configuration in Fig. 1. We first study the effect of the location of the outlet boundary on flow and heat transfer. Next, numerical results for $\mathrm{Gr} = 10^4$ and $\mathrm{Gr} = 10^5$ using the symmetric and the full domains are presented. Important differences and implications are highlighted.

2. Analysis

The total length of the heated horizontal surface (Fig. 1) is L, and its temperature is held constant at t_w. The reference ambient temperature is t_∞. The x and y coordinates are aligned as shown in the Fig. 2. The height of the enclosure is H which is set equal to its length, L. The gap between the horizontal plate and the bottom tip of the vertical wall is denoted by W. Air is blown through the opening from the top at a constant velocity, v_o. This boundary condition is realized in practice by a fan at the top of the enclosure.

Assuming laminar, incompressible flow, the governing equations of mass, momentum and energy conservation are applied to describe the flow and thermal transport in the partially open vertical enclosure. These, in non-dimensional form, are written as follows:

$$\frac{\partial U}{\partial X} + \frac{\partial V}{\partial Y} = 0, \tag{1}$$

$$\frac{\partial U}{\partial \tau} + U\frac{\partial U}{\partial X} + V\frac{\partial U}{\partial Y} = -\frac{\partial P}{\partial X} + \frac{1}{\sqrt{\mathrm{Gr}}}\nabla^2 U, \tag{2}$$

$$\frac{\partial V}{\partial \tau} + U\frac{\partial V}{\partial X} + V\frac{\partial V}{\partial Y} = -\frac{\partial P}{\partial Y} + \frac{1}{\sqrt{\mathrm{Gr}}}\nabla^2 V + T, \tag{3}$$

$$\frac{\partial T}{\partial \tau} + U\frac{\partial T}{\partial X} + V\frac{\partial T}{\partial Y} = \frac{1}{\mathrm{Pr}\sqrt{\mathrm{Gr}}}\nabla^2 T. \tag{4}$$

The non-dimensional parameters that appear in the formulation are the Grashof number, the Prandtl number and the Reynolds number. Note that although the Reynolds number does not appear in the equations explicitly, it does appear in the boundary conditions in the expression for the non-dimensional inlet velocity as $\mathrm{Re}/(\mathrm{Gr})^{1/2}$. The ratio $\mathrm{Gr}/\mathrm{Re}^2$ indicates the relative strengths of the two convective mechanisms.

Evaluation of Nusselt number: The local heat transfer coefficient h_x is defined as

$$q_x = h_x(t_w - t_\infty) = -k\left.\frac{\partial t}{\partial y}\right|_{y=0}. \tag{5}$$

The average heat transfer coefficient h is obtained by integrating Eq. (5) over the length of the horizontal surface (without the extension). The average Nusselt number Nu is defined as

$$\mathrm{Nu} = \frac{hL}{k} = \int_0^1 \left.\frac{\partial T}{\partial Y}\right|_{Y=0} \mathrm{d}X. \tag{6}$$

3. Numerical procedure

Eqs. (2)–(4) were solved to obtain the entire flow and temperature field using a commercially available finite element code, FIDAP (see FIDAP, 1996). An implicit variable timestep transient solver was employed for all computations except for fixing the location of the outlet boundary. Nine-node isoparametric quadrilateral elements were used. For this element, the velocity and temperature are approximated using biquadratic interpolation functions. For comparison, simulations were also performed using four-node quadrilateral bilinear elements. Qualitatively, the streamfunction and isotherm contours were identical. However, the results obtained using the four-node elements were different by a maximum of 4% from those obtained using nine-node elements. Since nine-node quadrilateral elements are known to be generally more accurate, they were used for all computations reported.

An implicit (backward-Euler) solution procedure was used for the transient calculations, as it allows for good stability.

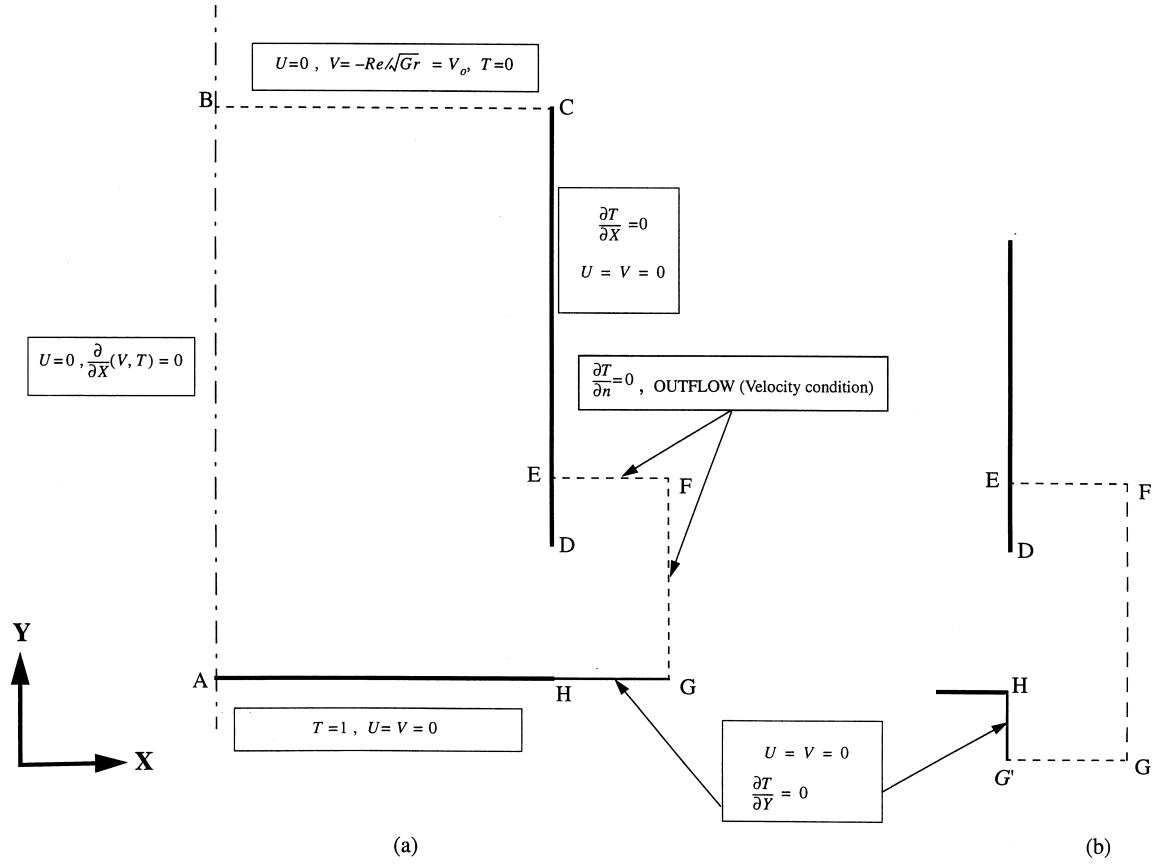

Fig. 2. Numerical boundary conditions: (a) horizontal extension, (b) vertical extension.

For selecting an appropriate value for the initial timestep, different values from 0.05 to 0.5 were tried. The best value was found to be 0.1. For values lower than this, there was no difference in the final result. However, for higher values, non-convergence was observed for certain cases. After an initial timestep is selected, the algorithm automatically adjusts the timestep based on the time history and the projected accuracy of the calculations (see FIDAP theory manual for details). The timestep usually grows rapidly as the solution approaches steady state. Steady state was assumed when the value of the non-dimensional timestep exceeded 5×10^5. The convergence criteria used was that the error residuals converge within 10^{-4} for the field quantities (U, V, and T).

A variable grid with a finer grid spacing near the hot surface and the exit was used. A grid dependence study was conducted to arrive at the appropriate size of the grid to combine accuracy and efficiency. The number of grid points was varied from 669, 1145, 2707, to 4515 for a typical set of operating conditions. It was observed that the field quantities and the Nusselt numbers varied less than 1% after the number of grid points was increased beyond 1145. A grid size 25×49 (1145 grid points) was chosen for all further computations.

In order to validate the procedure, a simulation was performed at $\mathrm{Gr}/\mathrm{Re}^2 = 100$, for $\mathrm{Gr} = 10^5$. The results of this simulation were compared with those obtained using the ADI-finite difference method (Calmidi and Mahajan, 1995). Streamfunction contours for this simulation are shown in Fig. 3. Clearly, there is an excellent agreement between the results generated by FIDAP and the ADI code. Further, the Nusselt numbers differed by less than 2% (8.23 using FIDAP, and 8.06 using ADI method).

4. Boundary conditions

As mentioned earlier, both the symmetric and the full domains were employed in this study. Each is described in detail below.

(a) *Symmetric domain*: Both the geometry and boundary conditions are symmetric about the vertical axis. Thus, in theory, the problem can be reduced by considering only one half of the domain and applying symmetry boundary conditions along the axis. This is shown in Fig. 2(a) along with the numerical boundary conditions.

The numerical domain is extended beyond the physical domain of interest (Markatos et al., 1982) and outflow conditions are specified at the exit plane of the extended domain. Following Calmidi and Mahajan (1995), two kinds of extensions are studied; HG in Fig. 2(a) (horizontal extension) and HG′ in Fig. 2(b) (vertical extension). Both are considered to be adiabatic. The length of the extensions is 10% of the overall length of the horizontal plate. In the absence of viscosity, location D is a point of singularity. Even though the flow considered here is not inviscid, it would still be difficult to specify realistic boundary conditions close to this point of potential singularity (which would be the case in the absence of the artificial domain extension). The length DE is fixed such that it is one half of the exit opening.

To underscore the importance of selecting the appropriate exit plane, we present plots of the horizontal velocity component at the exit plane of the physical domain, i.e., DH in Fig. 2(a),(b). These were obtained by solving the steady state equations to conserve time. Fig. 4 shows a plot of U at the exit plane (DH) for typical conditions. Clearly, the solution

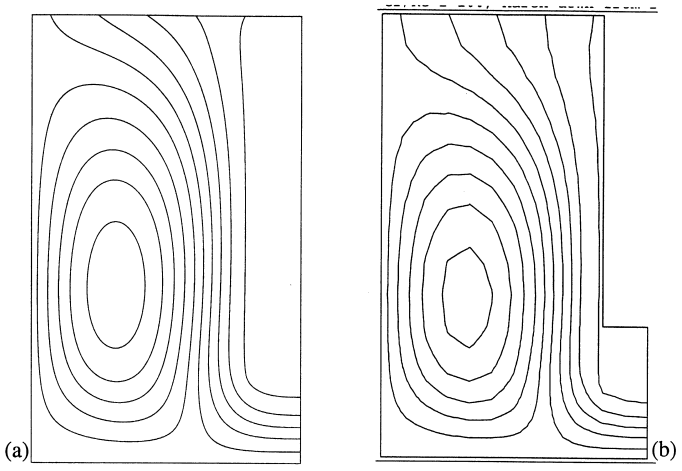

Fig. 3. Streamfunction contours of identical magnitude for $Gr = 10^5$, $Gr/Re^2 = 100$: (a) solution obtained using ADI method (Calmidi and Mahajan, 1995); (b) solution obtained using FIDAP (present study).

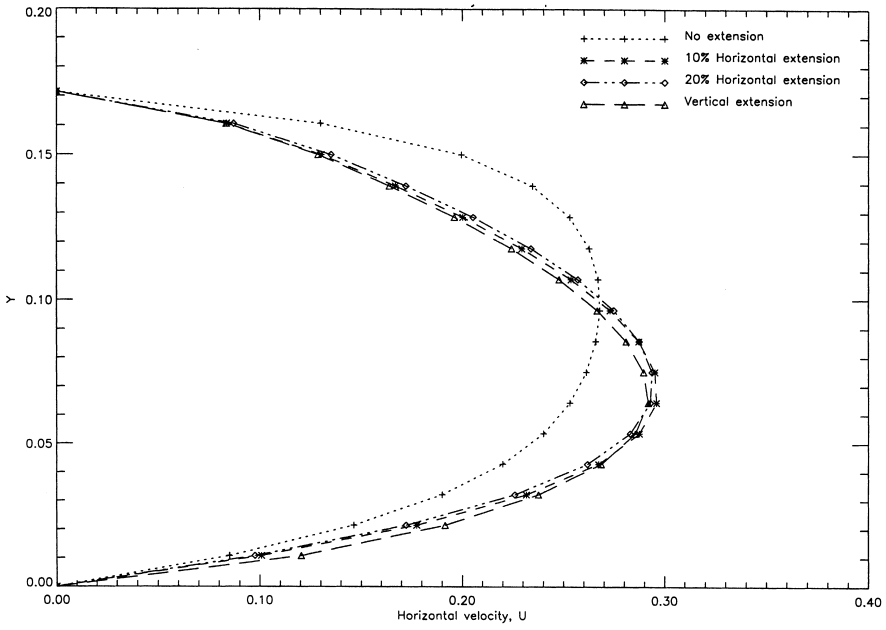

Fig. 4. Horizontal velocity component, U, at the exit plane of domain (DH in Fig. 2).

obtained without an artificial extension is very different from that obtained with the extensions. Table 1 shows the Nusselt numbers for the different extensions. Since the difference in the Nusselt number between the vertical extension and the horizontal extension is only 1.33%, a horizontal extension was chosen since it provided faster convergence rate The computations were repeated for an extension length of 20% and results were nearly identical (<1%) to those for the 10% extensions.

Table 1
Nusselt number for $Gr/Re^2 = 200$, $Gr = 10^5$

No artificial extension	Horizontal extension (10%)	Vertical extension (10%)
7.81	8.15	8.26

Thus a horizontal extension of 10% (of the length of the horizontal surface) was chosen for all further computations.

Numerical boundary conditions for the symmetric domain are summarized in Fig. 2(a). No-slip velocity conditions exist on the walls. The enclosure walls and the horizontal plate are isothermal. The constant flow enters the enclosure at ambient temperature. At the exit, heat conduction across the boundary is considered to be negligible compared to advection. The velocity condition at the exit is the stress-free boundary condition which is labeled as "outflow" in Fig. 2(a).

(b) *Full domain*: Here, no symmetry condition was imposed. The boundary conditions are identical to those for the symmetric domain, except that the boundary condition on the axis is absent and the full domain is simulated. The grid spacing was also chosen to be the same as in the symmetric case, i.e., the number of grid points was doubled. A horizontal extension of 10% was used.

5. Results

In this section, we describe the results for both $Gr = 10^4$ and 10^5 obtained using the symmetric domain as well as the full domain.

Case I (Marched solutions, symmetric domain, $Gr = 10^4$): This corresponds to varying the flow rate with the surface temperature held constant. Numerical calculations are presented for a range of values of Gr/Re^2, $10 < Gr/Re^2 < 350$ for $Gr = 10^4$. Prandtl number is 0.7. This whole range was traversed in two ways (see Fig. 5):

(a) Initially, $Gr/Re^2 = 10$ and successive solutions were obtained for increasing Gr/Re^2 (decreasing Re).

(b) Initially, $Gr/Re^2 = 350$ and successive solutions were obtained for decreasing Gr/Re^2 (increasing Re).

In all simulations, the final solution of a previous value of Gr/Re^2 was used as the initial condition for the current step. To obtain the first step ($Gr/Re^2 = 10$), the ambient (no flow) was used as the initial condition.

(a) *Marching from high Re to low Re*: Stream function and isotherm contours are shown in Fig. 6 for increasing values of Gr/Re^2. For high values of Re, conditions are clearly forced-flow dominated. As Re is decreased, a weak buoyancy induced cell begins to appear above the heated surface ($Gr/Re^2 = 150$). As Re is decreased further, the cell grows in size. Its growth saturates beyond $Gr/Re^2 = 200$.

Isotherms are shown in the bottom half of Fig. 6 just below the corresponding streamfunction contours. For higher values of Gr/Re^2, they indicate considerable similarity to classical buoyancy induced flow over a hot horizontal surface, especially in the region of recirculation where the effect of the forced flow is minimal. Substantial gradients can be seen in the central recirculating flow region. Outside this region, temperature gradients are negligible.

The Nusselt number plot shown in Fig. 5 is consistent with the flow and temperature fields discussed above. Starting at high Gr/Re^2, when the flowrate is decreased, the heat dissipated from the horizontal surface falls rapidly. This is because most of the heat is convected away by the incoming forced flow. Thus, a decrease in the flowrate results in a decrease in the Nusselt number. However, once the buoyancy driven cell begins to form, it transfers heat from the horizontal surface to the forced flow, thus isolating the forced flow from the hot surface. Now, the heat dissipated is related to the strength of the buoyancy driven cell. Since Gr is a constant, once a buoyancy driven cell fully establishes itself, its strength does not vary. Thus the value of the Nusselt number saturates beyond $Gr/Re^2 = 200$.

(b) *Marching from low Re to high Re*: Starting from a low value of Re ($Gr/Re^2 = 350$), solutions were obtained by gradually increasing the flowrate. Both the field quantities and the Nusselt number values were identical to the previous case (decreasing Re). Thus, no multiple steady states exist. This behavior is different from what was observed in the past for this configuration by Calmidi and Mahajan (1995), and for the MOCVD configuration (Kelkar et al., 1996; Patnaik et al., 1989; Fotiadis et al., 1987; Kelkar, 1996; Weber et al., 1990). Absence of multiple steady states for this study is probably due to low Grashof number (10^4) for which mixed convection interaction effects are small.

Case II (Marched solutions, full domain, $Gr = 10^4$): For the same conditions as in Case I, solutions were obtained using the full domain without imposing the symmetry condition along the centerline. However, no difference was observed between the symmetric and the full domains. Weber et al. (1990) observed asymmetries when they simulated the full domain for the MOCVD configuration. Once again, it is possible that the symmetric solutions are stable due to the small value of the Grashof number.

Case III (Marched solutions, symmetric domain, $Gr = 10^5$): To investigate whether the hysteresis effect observed by Patnaik et al. (1989) and Fotiadis et al. (1987) could be reproduced at higher Gr, simulations were performed at a higher Grashof number (10^5). As before, marched solutions were obtained.

(a) *Marching from high Re to low Re*: Stream function contours are shown in the top part of Fig. 7 for increasing values of Gr/Re^2. As in Case I, for high values of Re, conditions are clearly forced-convection dominated. As Re is decreased gradually, initially there is no substantial change in the flow pattern except for the reduced magnitude of the velocities. At $Gr/Re^2 = 60$, a strong buoyancy-driven cell suddenly appears in the enclosure. This is in contrast to Case I for $Gr = 10^4$ where the buoyancy cell developed gradually with decreasing Re. Isotherm contours are shown in the bottom part of Fig. 7. They are similar to Case I, except that the temperature gradients are higher because the Grashof number is higher.

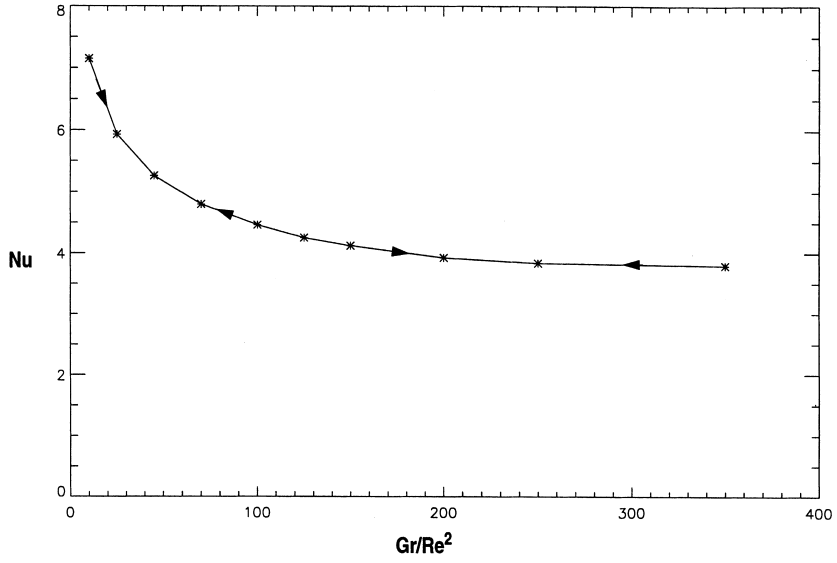

Fig. 5. Nusselt number as a function of Gr/Re^2 for $Gr = 10^4$ (symmetric domain).

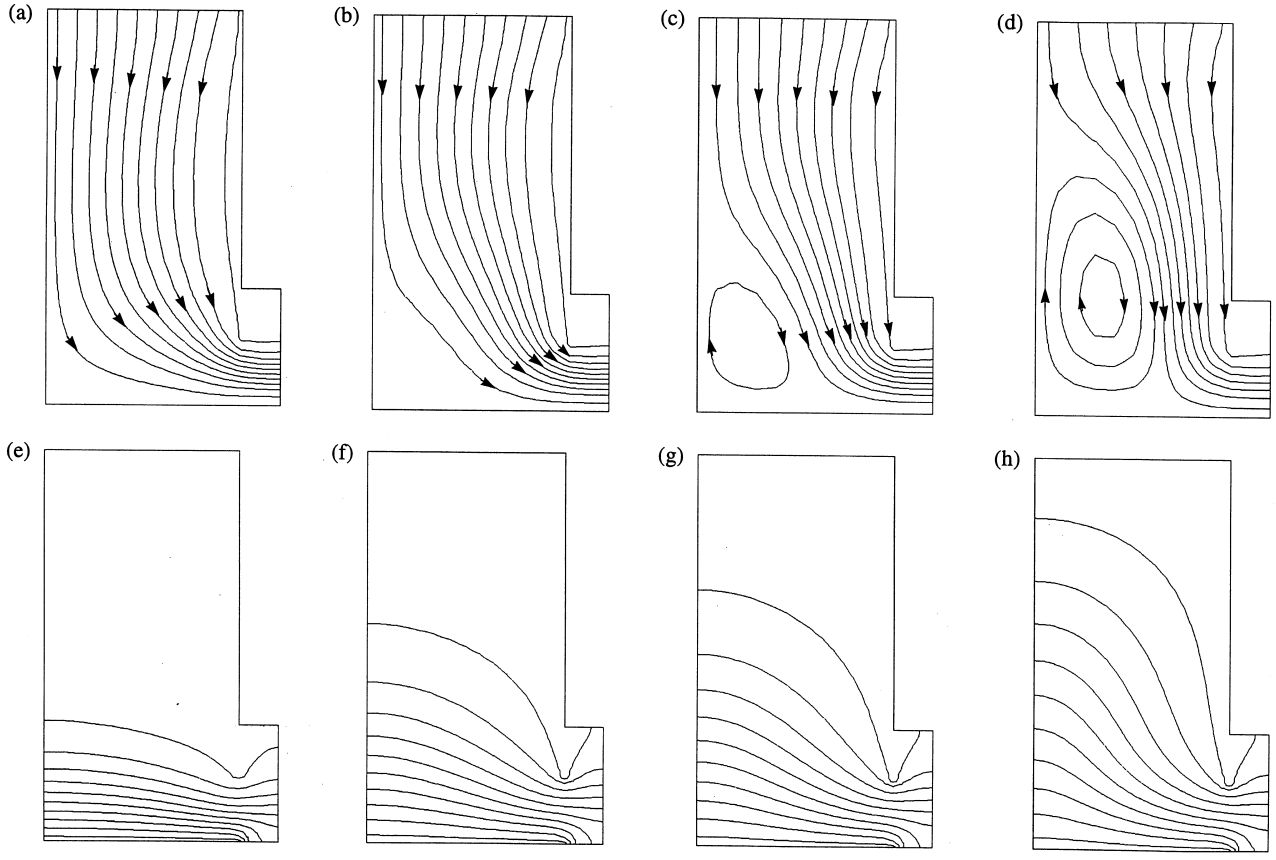

Fig. 6. Streamfunction (a–d) and isotherm (e–h) contours for decreasing (and increasing) Re ($Gr = 10^4$): (a) $Gr/Re^2 = 45$; (b) $Gr/Re^2 = 150$; (c) $Gr/Re^2 = 200$; (d) $Gr/Re^2 = 350$; (e) $Gr/Re^2 = 45$; (f) $Gr/Re^2 = 150$; (g) $Gr/Re^2 = 200$; (h) $Gr/Re^2 = 350$.

The Nusselt number dependence on Gr/Re^2 is shown in Fig. 8 by the solid line. Starting from high Re ($Gr/Re^2 = 10$), when Re is decreased, Nu also decreases. However, at $Gr/Re^2 = 60$, there is a sharp change in Nu because the flow pattern changes abruptly. The presence of the newly created strong buoyancy cell increases the heat convected away from the heated horizontal surface. When Re is decreased further, and the flowrate decreases, the strength of the buoyancy driven cell remains nearly a constant (because Gr is constant). Hence the Nusselt number reaches an asymptotic value and does not vary substantially.

(b) *Marching from low Re to high Re*: The Nu dependence on Gr/Re^2 is shown in Fig. 8 by the dotted line. Starting from $Gr/Re^2 = 100$, when flow is increased gradually, it follows the same path (as the solid line) till $Gr/Re^2 = 60$ where it deviates and follows a different path until $Gr/Re^2 = 28$. Beyond this, the two curves are identical.

Clearly, there is a hysteresis phenomenon similar to that observed for the MOCVD reactor by Patnaik et al. (1989) and Fotiadis et al. (1987) and for the present configuration by Calmidi and Mahajan (1995). Streamfunction and isotherm contours are shown in Fig. 9 for the same values of Gr/Re^2 as in Fig. 7. Multiple steady state solutions exist for the range of values given by $28 < Gr/Re^2 < 60$. The observed hysteresis is related to the appearance and disappearance of the cell in the two cases (decreasing and increasing Re respectively). We note from our calculations that as flow is decreased from $Gr/Re^2 = 10$, the buoyancy cell does not appear until $Gr/Re^2 = 60$. From this point, if the flow is increased, the buoyancy cell remains and does not disappear until $Gr/Re^2 = 28$.

From the two marched solutions presented above, the indication is that if a buoyancy induced cell already exists, it persists for long before disappearing. It requires a much larger value of forced flow rate to completely wipe it out. On the other hand, an established forced flow inhibits the formation of the buoyancy induced cell and causes the cell to appear at a much higher value of Gr/Re^2. To clarify the point further, we compare Fig. 9(c) and (g) with Fig. 7(b) and (f). They are for an identical set of conditions. While there is a fully established cell in Fig. 9(c), there is no such cell in Fig. 7(b). Also note that hysteresis is observed only when the buoyancy cell appears/disappears. Once the cell is present or has completely disappeared, the effect of initial conditions is not felt. This is clear from Fig. 8, where the two curves coincide. This phenomenon of hysteresis clearly suggests a complex nonlinear interaction between buoyancy induced and forced flows.

Case IV (Marched solutions, full domain, $Gr = 10^5$): The simulations in Case III were repeated, this time using the full domain to investigate its effect on the hysteresis and the presence of any asymmetries that have showed up in similar configurations (Kelkar, 1996; Weber et al., 1990).

(a) *Marching from high Re to low Re*: Starting from $Gr/Re^2 = 10$, as the Reynolds number is decreased, initially the solutions follows the same path as that of the symmetric domain (Case III). However, for $Gr/Re^2 \geqslant 60$, two new paths emerge neither of which is the one predicted using the symmetric domain (Fig. 8, solid line). Moreover, both these paths comprise of asymmetric flow patterns. They are labeled 'a' and 'b' in Fig. 10 which shows the dependence of Nu on Gr/Re^2. Each of the two paths is discussed separately below.

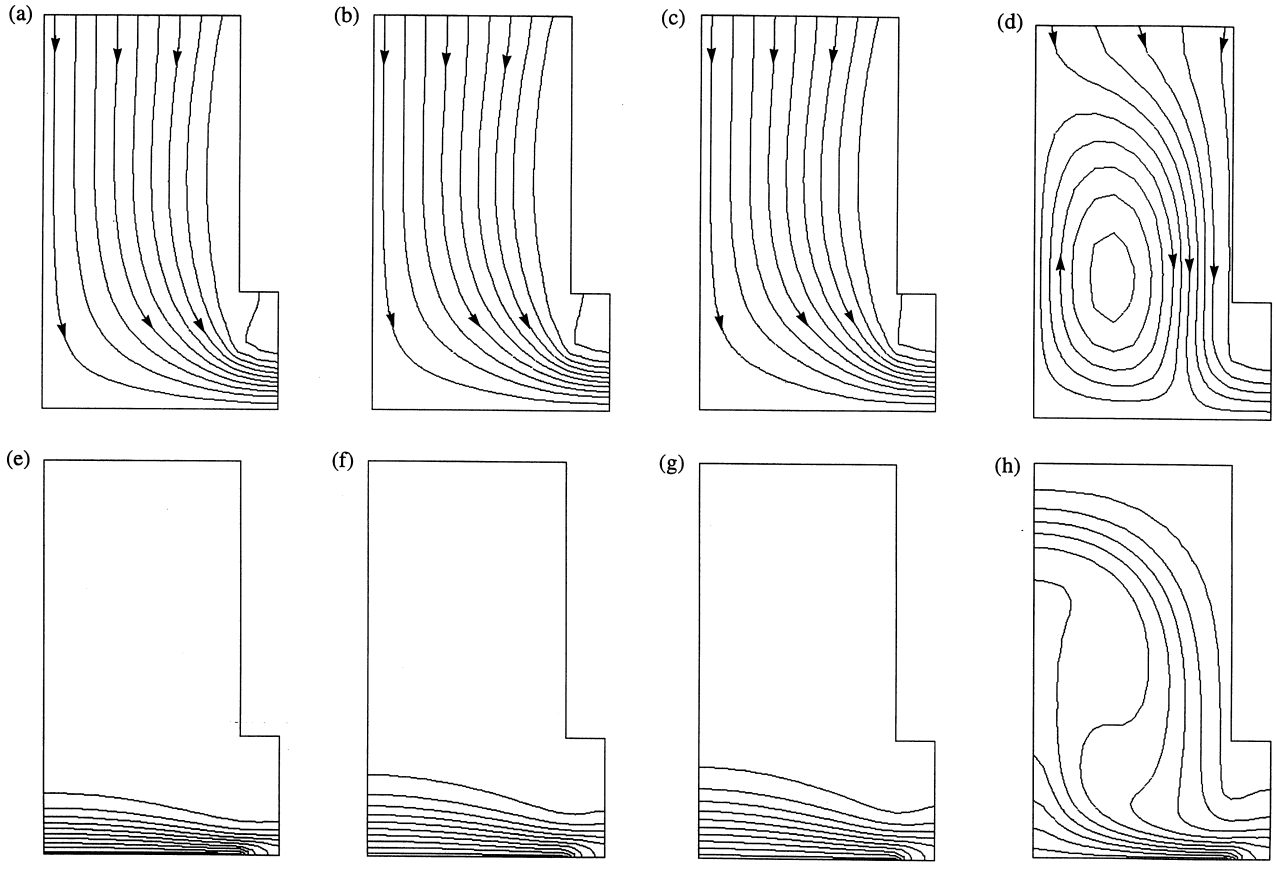

Fig. 7. Streamfunction (a–d) and isotherm (e–h) contours for decreasing Re ($Gr = 10^5$): (a) $Gr/Re^2 = 10$; (b) $Gr/Re^2 = 30$; (c) $Gr/Re^2 = 45$; (d) $Gr/Re^2 = 100$; (e) $Gr/Re^2 = 10$; (f) $Gr/Re^2 = 30$; (g) $Gr/Re^2 = 45$; (h) $Gr/Re^2 = 100$.

(i) Fig. 11(a) shows the streamfunction contours for $Gr/Re^2 = 60$ obtained using the converged steady state solution for $Gr/Re^2 = 50$ as the initial condition. The presence of a strong asymmetry is evident from the flow patterns. Using this as the initial condition and marching further yields flow patterns of the same type for higher values of Gr/Re^2 indicating that this is an entirely different branch. From Fig. 10, the Nusselt number remains nearly constant because most of the heat dissipated is due to the dominant buoyancy driven cell whose strength is independent of the incoming forced flow.

(ii) Fig. 11(b) shows the streamfunction contours for $Gr/Re^2 = 60$ obtained using the solution for $Gr/Re^2 = 55$ as the initial condition. A slight asymmetry is noticeable in the flow patterns. Further, this asymmetry grows with increasing values

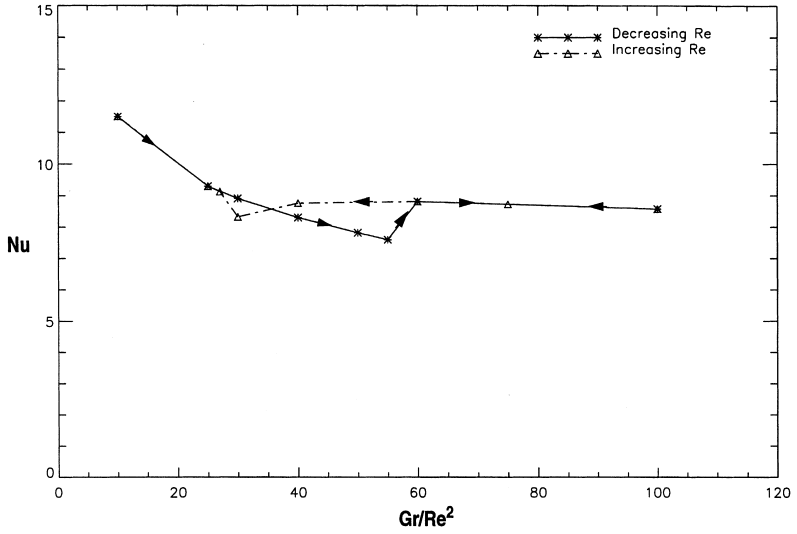

Fig. 8. Nusselt number as a function of Gr/Re^2 for $Gr = 10^5$ (symmetric domain).

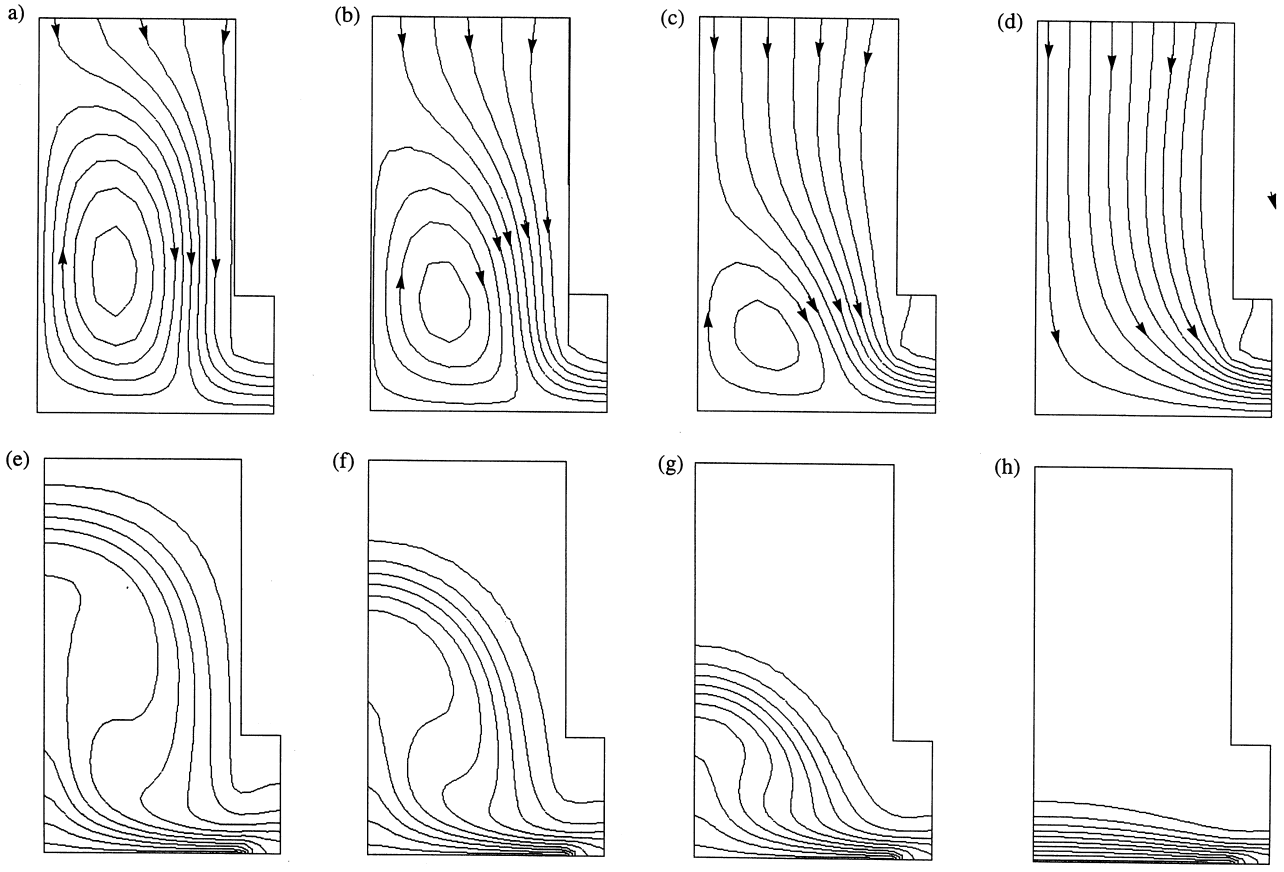

Fig. 9. Streamfunction (a–d) and isotherm (e–h) contours for increasing Re ($Gr = 10^5$): (a) $Gr/Re^2 = 100$; (b) $Gr/Re^2 = 45$; (c) $Gr/Re^2 = 30$; (d) $Gr/Re^2 = 10$; (e) $Gr/Re^2 = 100$; (f) $Gr/Re^2 = 45$; (g) $Gr/Re^2 = 30$; (h) $Gr/Re^2 = 10$.

of Gr/Re^2. The experimental results of de Keijser et al. (1988) and Roksnoer et al. (1989) show asymmetries similar to this kind in VPE reactors. From Fig. 10, the Nusselt number decreases with increasing values of Gr/Re^2. This is because there is no buoyancy-driven cell in the enclosure and the heat dissipated is primarily due to the forced flow which decreases in magnitude with increasing Gr/Re^2. In order to test for any grid dependencies, simulations in cases IV (a) and (b) were repeated using an overall mesh density which was one and a half times more refined. Identical results were obtained.

Recall that for the symmetric domain (Case III), the hysteresis loop closed at $Gr/Re^2 = 60$. For $Gr/Re^2 > 60$, the flow patterns consisted of a buoyancy driven cell each in the two symmetric halves of the enclosure. In this case, for $Gr/Re^2 > 60$, asymmetries begin to appear. This suggests that the symmetric branch for $Gr/Re^2 > 60$ predicted using the

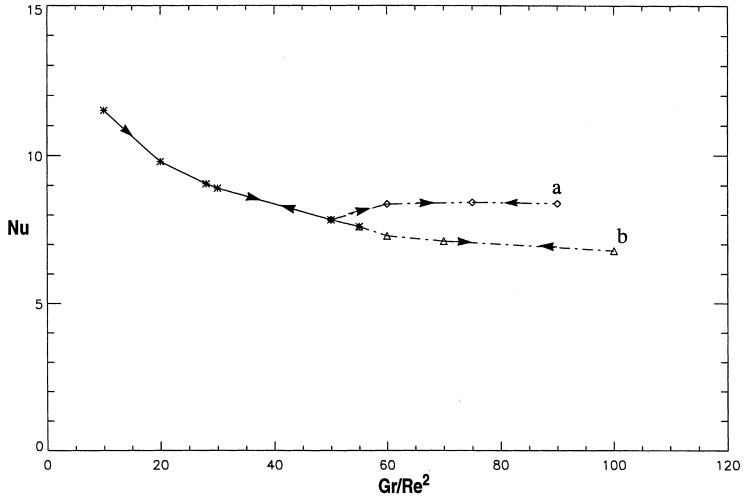

Fig. 10. Nusselt number as a function of Gr/Re^2 for $Gr = 10^5$ (symmetric domain).

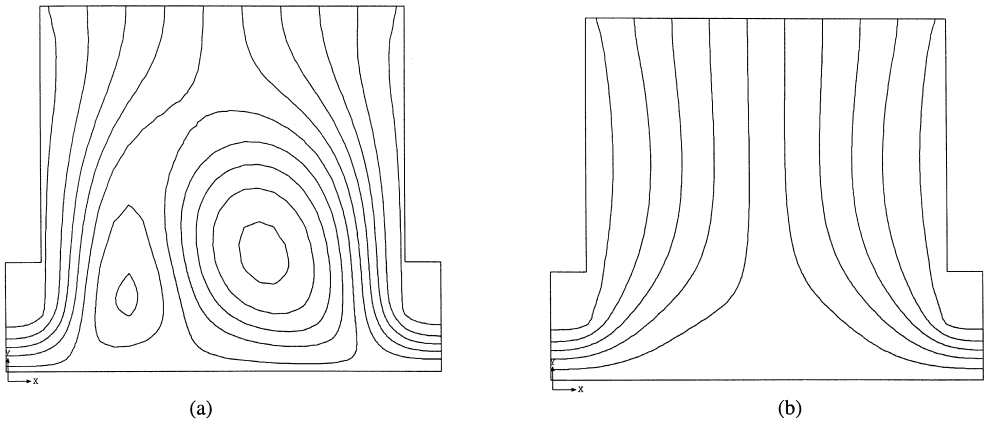

Fig. 11. Streamfunction contours using full domain for $Gr/Re^2 = 60$, $Gr = 10^5$: (a) solution from initial condition, $Gr/Re^2 = 50$; (b) solution from initial condition, $Gr/Re^2 = 55$.

symmetric domain (Case III) is unstable. That solution is perhaps stabilized artificially by the symmetry boundary condition.

(b) *Marching from low Re to high Re*: Starting from high Gr/Re^2, simulations were performed by gradually increasing the Reynolds number. For both the paths predicted in Case IVa, identical solutions were obtained for increasing Re too. Thus, contrary to the results in Case III, no hysteresis exists.

The results in Cases IVa,b indicate that the symmetric domain analysis may not be suitable for computation in certain domains of interest. The symmetry boundary condition not only seems to artificially stabilize the symmetric branch for high Gr/Re^2, but it also introduces the hysteresis effect, as a result.

The results presented above have important practical implications. For example, it was pointed out in the Introduction section that the flow configuration studied in this paper is very similar to that encountered in MOCVD reactors. Our results point out that the use of symmetric domain computations for the design or analysis of a MOCVD reactor is suspect. In our problem, both the symmetric and full domain solution for $Gr = 10^4$ are identical. The inference is that symmetric solutions are accurate for low Gr. However, for different geometric configurations, aspect ratios and Gr/Re^2 (Kelkar, 1996), the threshold value of Gr at which symmetric solutions are valid may be different. A safe bet, perhaps, is to use full domain solutions for these complex opposing mixed convection problems. In the context of MOCVD reactors, we also note that our full domain results indicate multi-branched solutions at higher Grashof numbers. This implies a potential instability in the operation of the MOCVD reactor. The suggestion is that the reactor should be operated at low values of Gr/Re^2 or at low values of Gr. Operating the reactor at low pressures is the preferred choice (in actual practice, the MOCVD reactors are operated at $\sim$80 Torr or less).

6. Summary

This paper presents a detailed numerical study of mixed convection over a heated horizontal surface in a partial enclosure. The objective of the study was to understand the effect of symmetry and exit boundary conditions.

The effect of the exit boundary was studied by artificially extending the exit boundary. Computations were performed at $Gr/Re^2 = 200$ and $Gr = 10^5$. It was found that choosing the correct location for the exit boundary is crucial to the accuracy of the quantitative results. In this case, the exit boundary was fixed after extending the domain horizontally by a length equal to 10% of the heated surface.

For detailed investigation of the presence of hysteresis effect and asymmetries, computations were performed for $Gr = 10^4$ and 10^5. For $Gr = 10^4$, both the symmetric and full domains yielded identical results and no hysteresis was observed. For $Gr = 10^5$, multiple steady state solutions were observed for both the symmetric and full domains indicating the possibility of more complex mixed convection interactions at higher Grashof numbers. However, hysteresis was observed for the symmetric domain analysis only. The full domain analysis yielded no hysteresis phenomena. In addition, two kinds of asymmetries were observed in the buoyancy dominated regime $Gr/Re^2 > 60$. The indication is that the application of the symmetry boundary condition artificially introduces the hysteresis phenomena and that care must be exercised in making use of this condition. Implications of these results to MOCVD reactors have also been discussed.

Acknowledgements

This work has been sponsored by CAMPmode, The Center for Advanced Manufacturing and Packaging of microwave, optical, and digital electronics at the University of Colorado.

References

Angirasa, D., Mahajan, R.L., 1995. Combined forced and buoyancy-induced convective heat transfer in a partially closed vertical channel. Numerical Heat Transfer, Part A (Applications) 27, 579–594.

Calmidi, V.V., Mahajan, R.L., 1995. Mixed convection on a horizontal surface within a partial enclosure: Hysteresis Effects. In: ASME Int. Mech. Eng. Conf. Exhib., San Francisco, HTD vol. 317, pp. 341–356.

Chen, L., Keyhani, M., Pitts, D.R., 1991. Convective heat transfer due to protruding heat sources in an enclosure. AIAA Journal of Thermophysics 5 (2), 217–223.

de Keijser, M., Opdorp, C., Weber, C., 1988. Peculiar asymmetric flow pattern in a vertical axisymmetric VPE reactor. J. Crystal Growth 92, 33–36.

FIDAP, 1996. Theory Manual. Fluid Dynamics International, Inc., Evanston, IL.

Fotiadis, D.I., Kremer, A.M., McKenna, D.R., Jensen, K.F., 1987. Complex flow phenomena in vertical MOCVD reactors: Effects on deposition uniformity and interface abruptness. J. Crystal Growth 85, 154–164.

Gebhart, B., Jaluria, Y., Mahajan, R.L., Sammakia, B., 1988. Buoyancy Induced Flow and Transport. Hemisphere, Washington, DC.

Hsu, T.H., Hsu, P.T., How, S.P., 1997. Mixed convection in a partially divided rectangular enclosure. Numerical Heat Transfer, Part A (Applications) 31 (6), 655–683.

Kelkar, A., 1996. Transport models for different MOCVD reactor configurations. Ph.D. Thesis, University of Colorado at Boulder.

Kelkar, A., Mahajan, R.L., Sani, R.L., 1996. Real-time physiconeural solutions for MOCVD. ASME J. Heat Transfer 118, 814–821.

Mahajan, R.L., 1996. Transport phenomena in chemical vapor-deposition systems. Adv. Heat Transfer 28, 339–425.

Markatos, N.C., Malin, M.R., Cox, G., 1982. Mathematical modeling of buoyancy-induced smoke flows in enclosures. Int. J. Heat Mass Transfer 25, 63–75.

Papanicolaou, E., Jaluria, Y., 1994. Mixed convection from simulated electronic components at varying relative positions in a cavity. ASME J. Heat Transfer 116, 960.

Patnaik, S., Brown, R.A., Wang, C.A., 1989. Hydrodynamic dispersion in rotating-disk OMVPE reactors: Numerical simulation and experimental measurements. J. Crystal Growth 96, 153–174.

Petersen, G.P., Ortega, A., 1990. Thermal control of electronic equipment and devices. Adv. Heat Transfer 20, 181–314.

Rahman, M.M., Carey, V.P., 1990. Experimental measurements of orthogonal mixed convection in a partial enclosure. Int. J. Heat Mass Transfer 33, 1307–1319.

Roksnoer, P.J., Opdorp, C., Maes, J.W.F.M., de Keijser, M., Weber, C., 1989. The effect of the asymmetric vortex in vertical VPE reactors on deposition nonuniformity. J. Electrochemical Soc. 136, 2427–2431.

Weber, C., Opdorp, C., de Keijser, M., 1990. Modeling of gas-flow patterns in a symmetric vertical vapor-phase-epitaxy reactor allowing asymmetric solutions. J. Appl. Phys. 67, 2109–2118.